Quantum Monte Carlo calculations of spectroscopic overlaps in $A \leqslant 7$ nuclei

I. Brida,[*] Steven C. Pieper,[†] and R. B. Wiringa[‡]

Physics Division, Argonne National Laboratory, Argonne, Illinois 60439, USA
(Received 15 June 2011; published 24 August 2011)

We present Green's function Monte Carlo calculations of spectroscopic overlaps for $A \leqslant 7$ nuclei. The realistic Argonne v_{18} two-nucleon and Illinois-7 three-nucleon interactions are used to generate the nuclear states. The overlap matrix elements are extrapolated from mixed estimates between variational Monte Carlo and Green's function Monte Carlo wave functions. The overlap functions are used to obtain spectroscopic factors and asymptotic normalization coefficients, and they can serve as an input for reaction calculations.

I. INTRODUCTION

One-nucleon spectroscopic overlaps, defined as the expectation value of the nucleon removal operator between states of nuclei differing by one particle, have been used in the treatment of processes in which one particle is added to or removed from the system [1,2]. In particular, these functions provide the interface between nuclear structure and direct reaction theories [3–6]. Traditionally, direct reaction theories of processes such as one-nucleon transfer, capture, knockout, or electron-induced proton knockout assume that the state of motion of only one particle is changed as a result of the projectile-target interaction, while the other particles are left essentially undisturbed. Under such a drastic approximation, the structure input needed to analyze experimental reaction data consists of single-particle-like functions of the involved nucleon inside the interacting nuclei, the one-nucleon overlaps.

For decades, direct reactions have been the main tool for extracting spectroscopic factors (SFs) defined as norms of spectroscopic overlaps. Given the single-particle-like nature of these overlaps, SFs are often associated with single-particle-level occupancies and compared mainly with shell-model values. In practical applications, "experimental" SFs are extracted from experimental cross sections in a model-dependent way with structure and reaction uncertainties entangled. This dependence was illustrated, for example, in Refs. [7,8], where SFs from transfer and electron-scattering data were shown to differ unless extracted in a consistent way. Strictly speaking, however, the overlaps and the SFs are merely theoretical concepts that cannot be measured. The overlaps should not be interpreted as the measurable probability amplitudes of finding a nucleon at some distance from the rest of the nucleus [9]. Nevertheless, until more advanced reaction models become available, spectroscopic overlaps and factors need to be calculated theoretically for a chosen Hamiltonian to enable the analysis of direct reaction data. These concerns are less severe for the long-range scaling factors of overlaps, the asymptotic normalization coefficients (ANCs), which enter the cross section of peripheral direct reactions, as these coefficients remain invariant under finite-range unitary transformations of the Hamiltonian [10]. The spectroscopic overlaps and factors are still useful to assess the relative importance of clustering patterns in a given nucleus.

Typically, spectroscopic overlaps are approximated by shell-model or mean-field single-particle functions, or they are taken as solutions of single-particle [Woods-Saxon (WS)] potential wells with some commonly accepted but otherwise arbitrary potential parameters [2,4,11]. Of a more recent vintage are some calculations attempting to account for contributions from missing model space, for example, results obtained within the correlated basis function theory [12] or overlaps generated as solutions of an inhomogeneous equation with a shell-model source term [13]. Realistic calculations of one-nucleon overlaps based on modern nuclear interactions are scarce and limited to light nuclei as they are complicated even in the simplest cases: In the s shell, they were computed in the hyperspherical harmonics (HH) method [14,15]; some overlaps and SFs for p-shell nuclei were calculated within the no-core shell model [16,17] and the coupled-cluster method [18]. Of particular relevance for the present work are previous variational Monte Carlo (VMC) overlap calculations for nuclei up to $A = 10$ (unpublished, available from Ref. [19]) and a more recent VMC-based calculation of ANCs in light nuclei [20]. VMC overlaps have been used in some analyses of hadronic [21–25] and leptonic [26] experiments.

This work provides a systematic study of one-nucleon spectroscopic overlaps, SFs, and ANCs in light nuclei calculated within the Green's function Monte Carlo (GFMC) method based on realistic two- and three-nucleon interactions. The GFMC method is designed to project the exact solutions out of trial wave functions by propagating them in imaginary time. The GFMC propagations are initiated by VMC wave functions. Over the years, the VMC/GFMC method has been found to accurately describe the structure and some reaction aspects of light nuclei [27–33]. Given our experience, GFMC is expected to improve VMC overlaps, especially in the p shell. In this paper, we present GFMC overlap results for nuclei up to $A = 7$; heavier nuclei up to $A \lesssim 10$ will be the subject of a forthcoming paper.

This paper is organized as follows. In Sec. II, the theoretical framework is established, the VMC and GFMC methods are briefly reviewed, and all overlap-related quantities are defined. Section III contains technical and computational details and an error analysis of the GFMC overlap calculations. Results

---

[*]brida@anl.gov

[†]spieper@anl.gov

[‡]wiringa@anl.gov

are presented and discussed in Sec. IV; final remarks and conclusions are given in Sec. V.

II. QUANTUM MONTE CARLO

To calculate spectroscopic overlaps, we first construct wave functions $\Psi(J^\pi, T, T_z)$ for nuclei of interest as solutions of the nonrelativistic many-body Schrödinger equation:

$$H\Psi(J^\pi, T, T_z) = E\Psi(J^\pi, T, T_z), \tag{1}$$

with J^π, T, and T_z denoting the total spin-parity, isospin, and isospin projection, respectively. The A-body Hamiltonians used in this work have the form

$$H = \sum_i^A K_i + \sum_{i<j}^A v_{ij} + \sum_{i<j<k}^A V_{ijk}, \tag{2}$$

where K_i is the nonrelativistic kinetic energy and v_{ij} and V_{ijk} are two-nucleon (2N) and three-nucleon (3N) potentials, respectively. Most of the results presented in this paper have been obtained for a combination of Argonne v_{18} (AV18) [34] 2N and Illinois-7 (IL7) [35] 3N realistic interactions. For benchmarking purposes, some calculations involved AV18 supplemented by the older Urbana IX (UIX) [36] 3N force. Our wave functions are translationally invariant and hence we have no spurious center-of-mass effects.

A. Variational Monte Carlo

The wave functions are constructed in two steps. First, a trial VMC approximation of Ψ, Ψ_V, is written and optimized by minimizing the energy expectation value as computed by Metropolis Monte Carlo integration [37]. Our latest variational functions have the form given by Eq. (3.13) of [38].

$$|\Psi_V\rangle = \mathcal{S} \prod_{i<j}^A \left[1 + U_{ij} + \sum_{k \neq i,j}^A \tilde{U}_{ijk}^{3N} \right] |\Psi_J\rangle. \tag{3}$$

The Jastrow wave function, Ψ_J, is a fully antisymmetric state having the desired J^π, T, T_z quantum numbers of the state of interest; the U_{ij} and $\tilde{U}_{ijk}^{3N}$ are two- and three-nucleon short-range correlation operators induced by dominant parts of 2N and 3N forces, respectively, while $\mathcal{S}$ is a symmetrization operator that restores the antisymmetry violated by the noncommuting character of U_{ij} and $\tilde{U}_{ijk}^{3N}$. At long range, appropriate boundary conditions are imposed on Ψ_V [39].

The Jastrow wave function for s-shell nuclei consists of a simple product of central pair and triplet correlation functions and an antisymmetrized spin-isospin state. For p-shell nuclei, we use two types of Ψ_J: a shell-model-like trial function, which we call type I, and a clusterized version denoted type II. These two kinds of wave functions differ primarily in their treatment of correlations between p-shell particles and the long-range asymptotics.

In type I trial functions, the single-particle radial functions of p-shell particles are exponentially decaying solutions of WS potential wells centered at the s-shell α core with potential parameters subject to a variational search. Pair correlations

between s- and p-shell particles and among p-shell particles themselves are chosen to allow clusterization in the p shell. Being less restrictive on long-range cluster decomposition compared with type II functions, type I functions are more widely applicable. Details of type I functions for nuclei with $A = 6, 7$ can be found in Ref. [40].

Type II functions that may be used for nuclei with low-lying cluster breakup thresholds impose a strict cluster-cluster asymptotic decomposition. Examples are the ground states of ^{6}Li and ^{7}Li that may asymptotically decouple into $\alpha + d$ and $\alpha + t$, respectively. In type II trial functions, the p-shell single-particle radial functions are again solutions of p-wave differential equations with potentials containing WS and Coulomb terms, but with an added Lagrange multiplier that turns on at long range. The role of the Lagrange multiplier is to impose the cluster boundary condition:

$$\Psi_V(r \to \infty) \propto \psi_\alpha \psi_x W_{-\eta, l+1/2}(2kr)/r, \tag{4}$$

where $x = d$ or t for ^{6}Li and ^{7}Li, respectively, and r and l are the relative α-x distance and orbital angular momentum. The Sommerfeld parameter η and the wave number k are related to the α-x separation energy in a given nucleus, which is set to its experimental value. Here, W is the Whittaker function defined in Eq. (13.1.33) of [41]. The correlations between p-shell particles in ^{6}Li and ^{7}Li are adopted from exact deuteron and variational triton wave functions, respectively. More details on type II trial functions are given in Refs. [32,42,43].

For either type of trial function, a diagonalization is carried out to find the optimal values of mixing parameters for states of different spatial symmetries among p-shell particles [27].

B. Green's function Monte Carlo

Being variational solutions of Eq. (1), the VMC wave functions Ψ_V can be improved further by action of the operator $\lim_{\tau \to \infty} \exp[-(H' - E_0)\tau]$, which, for a given set of quantum numbers, projects out the exact lowest-energy state Ψ_0 of a possibly simplified version H' of the desired Hamiltonian H. In practice, the operator is applied in small increments of the imaginary time τ up to some finite value to yield a propagated wave function $\Psi(\tau)$:

$$\Psi(\tau) = e^{-(H' - E_0)\tau} \Psi_V. \tag{5}$$

Obviously, $\Psi(\tau = 0) = \Psi_V$ and $\Psi(\tau \to \infty) = \Psi_0$. In practice, Eq. (5) is turned into an integral equation involving Green's functions with integrations performed by Monte Carlo methods; hence, the name GFMC. The energy E_0 is an approximate guess for the true eigenenergy corresponding to Ψ_0.

For a given state of the nucleus, quantities of interest are evaluated in terms of a "mixed" estimate between Ψ_V and $\Psi(\tau)$:

$$\langle O(\tau) \rangle_M = \frac{\langle \Psi(\tau) | O | \Psi_V \rangle}{\langle \Psi(\tau) | \Psi_V \rangle}. \tag{6}$$

The desired expectation values would have $\Psi(\tau)$ on both sides; by writing $\Psi(\tau) = \Psi_V + \delta\Psi(\tau)$ and neglecting terms of order

$[\delta\Psi(\tau)]^2$, we obtain the approximate expression

$$\langle O(\tau)\rangle = \frac{\langle\Psi(\tau)|O|\Psi(\tau)\rangle}{\langle\Psi(\tau)|\Psi(\tau)\rangle}$$
$$\approx \langle O(\tau)\rangle_M + [\langle O(\tau)\rangle_M - \langle O\rangle_V], \quad (7)$$

where $\langle O\rangle_V$ is the variational expectation value. The expectation value of H' is an exception to Eq. (7) because for this operator the mixed estimate already gives the correct value [27]. For off-diagonal matrix elements between two different A-body nuclear states, Eq. (7) can be generalized to a form involving two mixed estimates [32,33].

We note that the GFMC propagator involves a simplified Hamiltonian $H' = \mathrm{AV8}' + H'_{3N}$ based on a reprojection $\mathrm{AV8}'$ of the full AV18 two-body potential [40]. Therefore, the GFMC wave functions are really eigenstates of H' rather than H, which, in general, should not be a problem given that H' is a good approximation of H. In this work, the three-nucleon part H'_{3N} is either UIX or IL7, with the strength of their central repulsive parts adjusted so that $\langle H'\rangle \approx \langle H\rangle$. Although energies can be corrected perturbatively by adding $\langle H - H'\rangle$ to $\langle H'\rangle$, this kind of correction is not possible for other observables. In what follows, we refer to the desired Hamiltonian H remembering that, in fact, we use H' in GFMC propagations.

For a detailed description of the nuclear GFMC method, see the review [27] and references therein.

C. Spectroscopic overlaps and factors and asymptotic normalization coefficients

Let us consider a decomposition of an A-body nucleus, the parent, into the core C and a valence particle v (a proton or a neutron), namely, $A \rightarrow C + v$. The terms "core" and "valence" are used in a figurative sense considering that the parent wave functions are explicitly antisymmetrized states of indistinguishable particles. Then, a one-nucleon spectroscopic overlap is defined as a projection of a parent state onto an antisymmetrized core-valence product form,

$$R(\alpha, \gamma, v; r)$$
$$= C^{T_A T_{z,A}}_{T_C T_{z,C} t t_z} O(\alpha, \gamma, v; r)$$
$$\equiv \left\langle \mathcal{A}_{Cv}\left[[\Psi(\gamma; \xi_C) \otimes \mathcal{Y}(v; \hat{r}_{Cv}, \sigma_v, \tau_v)]_{J_A} \frac{\delta(r - r_{Cv})}{r^2_{Cv}} \right] \right.$$
$$\left. \times \middle| \Psi(\alpha; \xi_A) \right\rangle, \quad (8)$$

where $C^{T_A T_{z,A}}_{T_C T_{z,C} t t_z}$ is an isospin Clebsch-Gordan coefficient; $\alpha \equiv \{A, J_A^\pi, T_A, T_{z,A}\}$, $\gamma \equiv \{C, J_C^\pi, T_C, T_{z,C}\}$, and $v \equiv \{v, l, s, j, t, t_z\}$ are composite indexes for the parent, the core, and the valence particle, respectively; ξ comprise all degrees of freedom in a given nucleus; $\vec{r}_{Cv}$ is the vector extending from the core's center of mass to the valence particle; and $\mathcal{A}_{Cv}$ is the core-valence antisymmetrizer: $\mathcal{A}_{Cv} = (1/\sqrt{A})\sum_1^{A-1}(-1)^p P_{Cv}$ with P_{Cv} being the permutation operators exchanging the valence particle with those inside the core and p determining the permutation parity ± 1. The

symbols A and $C = A - 1$ also denote the nuclear mass numbers, and the subscripts A and C may be dropped when convenient. In Eq. (8), the parent and core states are assumed to be normalized to unity, and the integral is done over all $3(A - 1)$ internal coordinates of the parent nucleus. The valence angle-spin-isospin function is defined as

$$\mathcal{Y}(v; \hat{r}_{Cv}, \sigma_v, \tau_v) \equiv [Y_l(\hat{r}_{Cv}) \otimes \chi_s(\sigma_v)]_j \chi_{t,t_z}(\tau_v), \quad (9)$$

where Y_l is a spherical harmonic, $\chi_s(\sigma_v)$ and $\chi_{t,t_z}(\tau_v)$ denote the valence spin and isospin states with $s = t = 1/2$, respectively, and t_z gives the valence isospin projection $\pm 1/2$. Taking into account the antisymmetry of the parent state, one can turn the integral in Eq. (8) into a simpler form:

$$R(\alpha, \gamma, v; r) = \sqrt{A}\left\langle [\Psi(\gamma) \otimes \mathcal{Y}(v)]_{J_A}\left|\frac{\delta(r - r_{Cv})}{r^2_{Cv}}\right|\Psi(\alpha)\right\rangle. \quad (10)$$

By definition (8) and by using translationally invariant wave functions Ψ, the overlap functions R are translationally invariant. For a given parent-core combination, different angular momentum channels will be denoted l_j.

The theoretical SF is then defined as the norm of the overlap:

$$S(\alpha, \gamma, v) = \int |R(\alpha, \gamma, v; r)|^2 r^2 \, \mathrm{d}r. \quad (11)$$

Among other sum rules, all possible (proton, neutron) SFs for a given state of the parent nucleus add up to the parent's number of nucleons (protons, neutrons) [1]. Our definition of SFs is consistent with those of some other works, for example, Ref. [13], but differs from others [4,44] by inclusion of the isospin Clebsch-Gordan coefficient in Eq. (8) into overlaps and consequently into SFs [these works define SFs as norms of $O(r)$ in Eq. (8)].

To calculate the overlap functions R within GFMC, one can, neglecting terms of order $[\Psi(\alpha; \tau) - \Psi_V(\alpha)]^2$ and $[\Psi(\gamma; \tau) - \Psi_V(\gamma)]^2$, derive the following expression similar to Eq. (19) in Ref. [32]:

$$R(\alpha, \gamma, v; r; \tau)$$
$$= \sqrt{A}\frac{\left\langle [\Psi(\gamma; \tau) \otimes \mathcal{Y}(v)]_{J_A}\left|\frac{\delta(r - r_{Cv})}{r^2_{Cv}}\right|\Psi(\alpha; \tau)\right\rangle}{\sqrt{\langle|\Psi(\gamma; \tau)|^2\rangle}\sqrt{\langle|\Psi(\alpha; \tau)|^2\rangle}}$$
$$\approx \langle R(\alpha, \gamma, v; r; \tau)\rangle_{M_A} + \langle R(\alpha, \gamma, v; r; \tau)\rangle_{M_C}$$
$$\quad - \langle R(\alpha, \gamma, v; r)\rangle_V, \quad (12)$$

where

$$\langle R(\alpha, \gamma, v; r; \tau)\rangle_{M_A}$$
$$= \sqrt{A}\frac{\left\langle [\Psi_V(\gamma) \otimes \mathcal{Y}(v)]_{J_A}\left|\frac{\delta(r - r_{Cv})}{r^2_{Cv}}\right|\Psi(\alpha; \tau)\right\rangle}{\langle\Psi_V(\alpha)|\Psi(\alpha; \tau)\rangle}\sqrt{\mathcal{N}}, \quad (13)$$

$$\langle R(\alpha, \gamma, v; r; \tau)\rangle_{M_C}$$
$$= \sqrt{A}\frac{\left\langle [\Psi(\gamma; \tau) \otimes \mathcal{Y}(v)]_{J_A}\left|\frac{\delta(r - r_{Cv})}{r^2_{Cv}}\right|\Psi_V(\alpha)\right\rangle}{\langle\Psi(\gamma; \tau)|\Psi_V(\gamma)\rangle}\sqrt{\frac{1}{\mathcal{N}}}, \quad (14)$$

$$\langle R(\alpha, \gamma, \nu; r)\rangle_V$$

$$= \sqrt{A}\,\frac{\left\langle [\Psi_V(\gamma) \otimes \mathcal{Y}(\nu)]_{J_A} \left| \frac{\delta(r - r_{Cv})}{r_{Cv}^2} \right| \Psi_V(\alpha) \right\rangle}{\langle \Psi_V(\alpha)|\Psi_V(\alpha)\rangle}\,\sqrt{\mathcal{N}},$$

$$(15)$$

with a self-normalization factor:

$$\mathcal{N} = \frac{\langle \Psi_V(\alpha)|\Psi_V(\alpha)\rangle}{\langle \Psi_V(\gamma)|\Psi_V(\gamma)\rangle}. \qquad (16)$$

The overlap function $\langle R\rangle_V$ in Eq. (15) is a pure variational estimate, to be called a VMC overlap, whereas the other two estimates, $\langle R\rangle_{M_A}$ in Eq. (13) and $\langle R\rangle_{M_C}$ in Eq. (14), involve combinations of GFMC-propagated and VMC wave functions, and as such will be called A- and (A-1)-body mixed overlaps and referred to by the corresponding GFMC-propagated nucleus. For each estimate [Eqs. (13)–(15)] one can define a SF similar to Eq. (11). The GFMC-extrapolated overlap R in Eq. (12) is called a GFMC overlap. Obviously, at $\tau = 0$, $R = \langle R\rangle_V = \langle R\rangle_{M_A} = \langle R\rangle_{M_C}$.

Overlap functions R satisfy a one-body Schrödinger equation with the appropriate source terms [2]. Asymptotically, for $r \to \infty$, these source terms contain core-valence Coulomb interaction at most, and, hence, the long-range part of overlap functions for parent states below core-valence separation thresholds is proportional to a Whittaker function $W_{-\eta, l+1/2}$:

$$R(\alpha, \gamma, \nu; r) \xrightarrow{r \to \infty} C(\alpha, \gamma, \nu)\frac{W_{-\eta, l+1/2}(2kr)}{r}, \qquad (17)$$

where $\eta = Z_C Z_v (e^2/\hbar c)\sqrt{\mu c^2/2B}$ depends on proton numbers Z_C and Z_v and the core-valence reduced mass μ and separation energy B (positive for parent states below core-valence separation thresholds). The wave number k is defined as $\sqrt{2\mu B}/\hbar$, and l is the orbital angular momentum from Eq. (9). Note that W, μ, B, and k implicitly carry channel labels α, γ, and ν. The Whittaker function is defined in Eq. (13.1.33) of Ref. [41], and it has an (approximately) exponentially decaying tail. The proportionality constant $C(\alpha, \gamma, \nu)$ in Eq. (17) is the ANC.

To provide a convenient parametrization of overlaps suitable for reaction calculations and to extract ANCs, we perform χ^2 fits of the overlaps by the eigenstates of a single-particle-like Hamiltonian $-[\hbar^2/2\mu]\Delta + V(r)$ containing a WS plus spin-orbit (so) plus Coulomb (Coul) potential,

$$V(r) = V_{\mathrm{WS}}\left\{\frac{1}{1 + \exp[(r - R_{\mathrm{WS}})/a_{\mathrm{WS}}]} - \beta\exp[-(r/\rho)^2]\right\}$$
$$+ (4\vec{l} \cdot \vec{s})\frac{V_{\mathrm{so}}}{r}\frac{\mathrm{d}}{\mathrm{d}r}\left\{\frac{1}{1 + \exp[(r - R_{\mathrm{so}})/a_{\mathrm{so}}]}\right\} + V_{\mathrm{Coul}},$$

$$(18)$$

with

$$V_{\mathrm{Coul}} = \begin{cases} Z_C Z_v e^2/r & : r \geqslant R_{\mathrm{Coul}}, \\ Z_C Z_v e^2[3 - (r/R_{\mathrm{Coul}})^2]/[2R_{\mathrm{Coul}}] & : r < R_{\mathrm{Coul}}. \end{cases}$$

$$(19)$$

The central WS part of the potential includes a Gaussian "wine-bottle" term to provide an additional flexibility at short range. The depths V_{WS} and V_{so} are in the same units, the factor 4

in the spin-orbit part is approximately twice the square of the pion Compton wavelength $\hbar/(m_\pi c)$ in fm, and $\vec{l}$ and $\vec{s}$ are operators of the core-valence orbital angular momentum and of the valence spin, respectively, both in units of $\hbar$. The Coulomb radius is $R_{\mathrm{Coul}} = 2$ fm. The potential parameters are varied freely to provide the best fit under the constraint of the eigenenergy being equal to the desired value $-B$. This fitting procedure provides good overlap fits at short and medium distances; at large distances, the fits have the desired form shown in Eq. (17). These overlap parametrizations can be used in reaction codes such as PTOLEMY [45] or FRESCO [46], and they will be referred to as WS fits throughout the paper.

III. INNER WORKINGS OF OVERLAP CALCULATIONS AND ERROR ANALYSIS

In this section, we elaborate on some technical aspects of the overlap calculations, show several detailed examples, and assess systematic errors of quantities being computed. The discussion of results is given in Sec. IV.

The VMC overlap $\langle R\rangle_V$ in Eq. (15) is calculated on a random walk guided by the parent's $|\Psi_V(\alpha)|^2$. On the same walk, we also evaluate the self-normalization factor from Eq. (16); to extend the denominator of $\mathcal{N}$ into the space being sampled: (1) $\Psi_V(\gamma)$ is replaced by $\Psi_V(\gamma) \times p(\vec{r}_{Cv})$, where $p(\vec{r}_{Cv})$ acts as a single-particle function of a virtual valence particle taken with respect to the core's center of mass, and (2) the integral is extended to include $\vec{r}_{Cv}$. By requiring $\int p^2(\vec{r}_{Cv})\,\mathrm{d}\vec{r}_{Cv} = 1$, the original value of the denominator of $\mathcal{N}$ is preserved. In principle, any function can be used for p as long as the product form $|\Psi_V(\gamma) \times p|^2$ is a reasonably good approximation of the sampling probability density to yield reasonably small statistical errors on the denominator of $\mathcal{N}$. In practice, we find it sufficient to use purely radial (s-wave) functions $p(r_{Cv})$ of either a Gaussian shape or one generated by a single-particle-like Hamiltonian containing a WS potential well with parameters adjusted to minimize the error on $\mathcal{N}$. The WS-generated single-particle functions provide the advantage of $|\Psi_V(\gamma) \times p|^2$ being a better approximation of the sampling density at large core-valence distances, especially when the potential depth is set to approximately reproduce the (experimental or VMC) core-valence separation energy. In the present work, the self-normalization factors $\mathcal{N}$ were calculated (after accounting for autocorrelations between local samples) with an accuracy of the order of 0.1% or better.

The two mixed overlaps in Eqs. (13) and (14) are calculated on random walks guided by GFMC propagations for the corresponding nucleus. For the (A-1)-body mixed overlap, the GFMC sampling density only spans the core's subspace of the full space of the parent nucleus; we draw the position of the valence nucleon from the same single-particle density $p^2(\vec{r}_{Cv})$ used in the computation of the variational self-normalization factor $\mathcal{N}$.

Generating new VMC or GFMC samples is computationally more expensive than evaluating a sample's contribution to Eqs. (13)–(15). Therefore, to improve the computational efficiency, each VMC or GFMC sample is used several times: In Eqs. (13) and (15), we consider all A cyclic particle
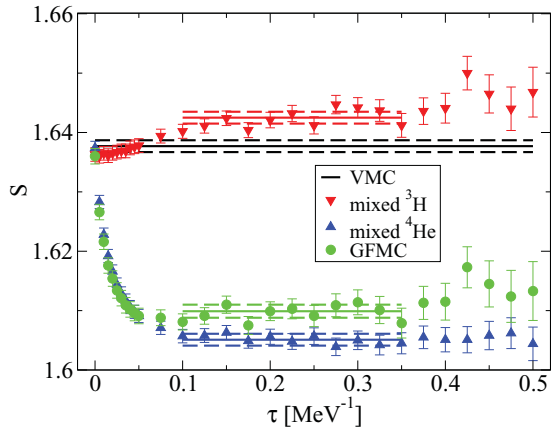
FIG. 1. (Color online) Imaginary time evolution of SFs in the $s_{1/2}$ channel of the $\langle^3\text{H}\,|\,^4\text{He}\rangle$ overlap obtained for the AV18 + IL7 potential. Only statistical errors are shown. Horizontal lines are SFs for VMC and time-averaged mixed and GFMC overlaps, as described in the text.

permutations to rotate the valence particle over all possible positions within the parent nucleus, while in Eq. (14) the position of the valence particle is drawn several (A) times from its single-particle distribution p^2 described above for each core's GFMC sample.

We illustrate the method with the $\langle^3\text{H}\,|\,^4\text{He}\rangle$ overlap for AV18 + IL7 taken as a typical example of overlaps in the s shell. First, the VMC overlap is computed by Eq. (15). Then, the wave functions of the parent and the core are independently propagated and the two mixed and the GFMC overlaps are computed in each radial bin following Eqs. (13), (14), and (12). The corresponding SFs are plotted in Fig. 1. In all figures, the quantities corresponding to the variational, the (A-1)- and the A-body mixed, and to the GFMC overlaps are plotted as black, red, blue, and green, respectively.

For s-shell nuclei, we do unconstrained propagations [40] and thus obtain essentially exact solutions for a given

Hamiltonian H' in Eq. (5). Because of the fermion sign problem, the statistical noise grows with time, as can be inferred from Fig. 1. Fortunately, GFMC quickly eliminates excited-state impurities from VMC wave functions resulting in a rapid convergence of mixed and GFMC overlaps and SFs. For s-shell nuclei, GFMC propagations are fully converged long before $\tau = 0.5$ MeV^{-1}, at which point they are terminated to avoid the increasing statistical noise.

To improve the statistical accuracy further, the (A-1)- and A-body mixed overlaps are separately averaged over time. These mixed time averages are then combined with the VMC overlap to obtain the final time-averaged GFMC overlap from Eq. (12). In Fig. 1 and similar figures, the variational estimate, although computed at $\tau = 0$ MeV^{-1}, is plotted across the full range of times, while the other solid lines give SFs for time-averaged mixed and GFMC overlaps with averaging done over the range of times indicated by the horizontal extent of these lines; the dashed lines show statistical errors. We have checked that our time-averaged results have little dependence on the exact time interval being averaged over as long as this interval is safely within the GFMC converged region and does not include large τ's for unconstrained propagations.

In Fig. 2, the VMC and time-averaged mixed and GFMC $\langle^3\text{H}\,|\,^4\text{He}\rangle$ overlaps are shown along with the asymptotic Whittaker function corresponding to the experimental separation energy (discussed below), a WS fit to the GFMC overlap, and the radial sampling probability. In general, the differences between s-shell VMC and time-averaged mixed and GFMC overlaps in a given overlap channel are very small because the starting VMC wave functions are already very good approximate solutions of Eq. (1); these small differences are reflected by small ($\sim$2%) differences between VMC and GFMC SFs, as illustrated in Fig. 1. Statistical errors on SFs are small because the dominant contribution to Eq. (11) comes from the volume region well covered by the Monte Carlo sampling probability, also shown in Fig. 2.

Overlaps between p-shell nuclei are computed by using the same algorithm with some technical modifications. Compared
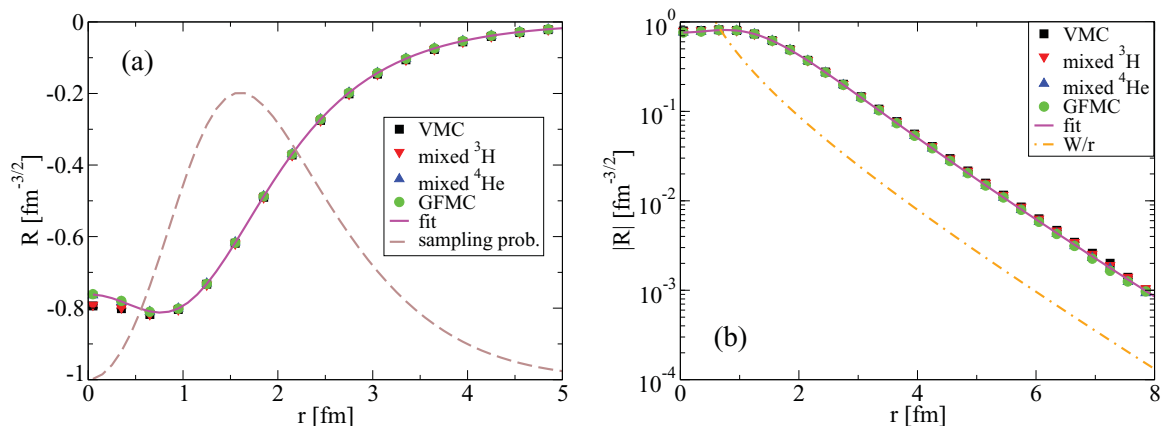

FIG. 2. (Color online) Linear (a) and logarithmic (b) plots of VMC and time-averaged mixed and GFMC $s_{1/2}\langle^3\text{H}\,|\,^4\text{He}\rangle$ overlaps obtained for the AV18 + IL7 potential. Only statistical errors are shown. Also shown in (b) are a WS fit to the GFMC overlap and the asymptotic Whittaker function corresponding to the experimental separation energy. Superimposed in the linear plot is the sampling probability (arbitrary scale).
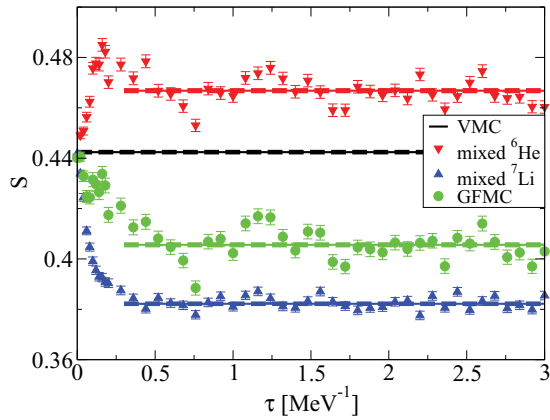
FIG. 3. (Color online) Imaginary time evolution of SFs in the $p_{3/2}$ channel of the $\langle {}^6\text{He}(0^+) \, | \, {}^7\text{Li}(3/2^-) \rangle$ overlap obtained for the AV18 + IL7 potential. The GFMC wave functions originated from type I VMC wave functions. Only statistical errors are shown. Horizontal lines are SFs for VMC and time-averaged mixed and GFMC overlaps, as described in the text.

with s-shell nuclei, the fermion sign problem becomes more severe in the p-shell, and we retreat to constrained path GFMC sampling [38]. Consequently, statistical errors are well under control, as illustrated in Fig. 3 for SFs in the $p_{3/2}$ channel of the $\langle {}^6\text{He}(0^+) \, | \, {}^7\text{Li}(3/2^-) \rangle$ overlap. Given our experience indicating that mixed estimates of many observables tend to fluctuate more in the p shell than in the s shell, we chose to carry out propagations for longer times up to $\tau = 3$ MeV^{-1} to ensure full convergence in the p shell. VMC and time-averaged mixed and GFMC overlaps corresponding to Fig. 3 are shown in Fig. 4. The difference of about 8% between the VMC and GFMC SFs reflects the change in the shape of the underlying overlaps.

At short range, the GFMC overlap is a result of fine cancellations between VMC and mixed overlaps in Eq. (12). At large core-valence distances, the GFMC overlaps tend to follow the A-body mixed overlaps, while the $(A-1)$-body

mixed overlaps usually stay close to the VMC ones, in agreement with our expectation that it is the long-range falloff of the parent's wave function that primarily sets the tail of the overlap, whereas the detailed structure of the core plays a less important role in this region although the core still needs to be described reasonably well. From this point on, mixed overlaps and estimates are not shown, and the time-averaged GFMC overlap is called a GFMC overlap.

Because of the vanishing sampling probabilities at large distances (an example is shown in Fig. 2), reliable sampling of overlap tails requires very large Monte Carlo sets; we propagated about 12×10^6 samples in the s shell and about 250 000 for p-shell nuclei. As a consequence, statistical errors are small. It is therefore important to assess systematic errors in addition to statistical errors. The most notable sources of systematic errors are the difference between the Hamiltonian H' in the GFMC propagator in Eq. (5) and the desired H in Eq. (1), possible errors owing to the constrained path sampling in the p shell, and a residual dependence of GFMC results on starting VMC wave functions. In addition, ANCs depend on the separation energy used in their determination. We now attempt to place limits on such systematic errors.

For s-shell nuclei, we can compare our results with those obtained by the HH method [14,15,47,48]. For AV18 + UIX, the agreement between HH and GFMC is very good, as can be seen from Fig. 6 for overlaps and from Table IV for SFs in Sec. IV. Testing the bias owing to H' for p-shell overlaps is not possible because, to our knowledge, no p-shell overlaps have been published previously for the realistic interactions employed here. To test the dependence of GFMC SFs on VMC wave functions, we include in Table V results involving the ground state of ${}^7\text{Li}$ obtained for several combinations of types I and II (see Sec. II A) trial wave functions. Although VMC SFs for different Ψ_V may differ by as much as 20%, GFMC reduces the spread to no more than 3%. Hence, we estimate systematic errors on GFMC SFs to be no more than 2–3%.

Typically, extracting ANCs directly from overlaps in Eq. (10) is problematic for most many-body methods. First,
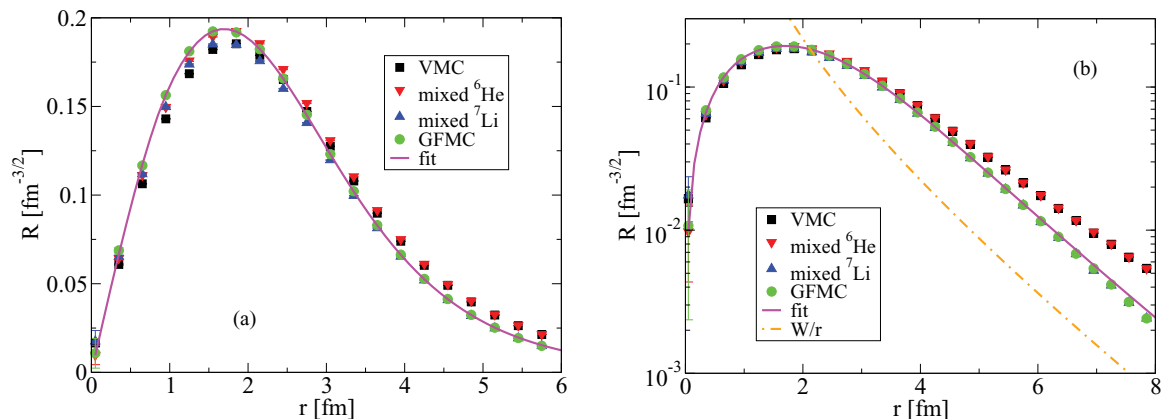

FIG. 4. (Color online) Linear (a) and logarithmic (b) plots of VMC and time-averaged mixed and GFMC $p_{3/2} \langle {}^6\text{He}(0^+) \, | \, {}^7\text{Li}(3/2^-) \rangle$ overlaps obtained for the AV18 + IL7 potential. The GFMC wave functions originated from type I VMC wave functions. Only statistical errors are shown. Also shown are a WS fit to the GFMC overlap and the asymptotic Whittaker function corresponding to the experimental separation energy in the logarithmic plot.
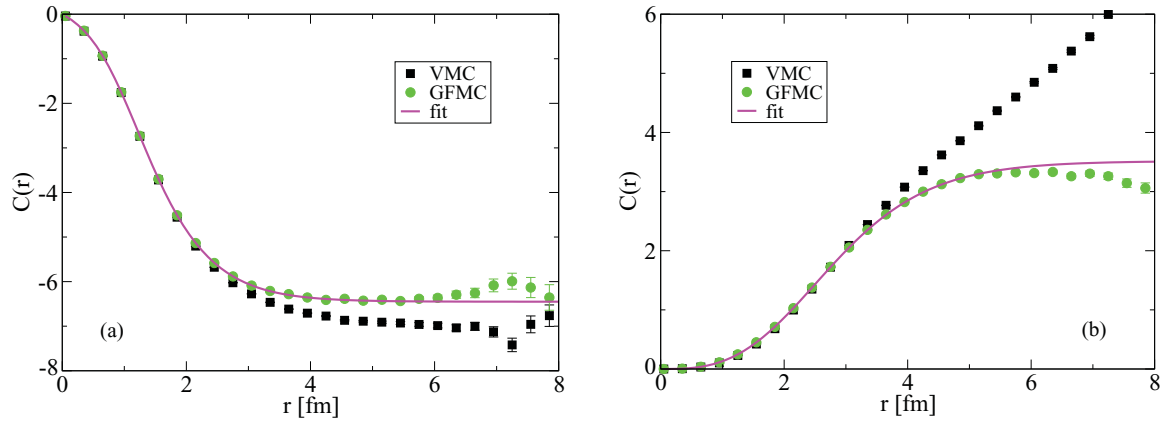
FIG. 5. (Color online) The ratio $C(r)$ of VMC, GFMC, and fitted GFMC overlaps to asymptotic Whittaker functions. The WS fits and the Whittaker functions assume experimental core-valence separation energies. (a) $\langle ^3\text{H} \,|\, ^4\text{He}\rangle$ overlaps from Fig. 2; (b) $\langle ^6\text{He}(0^+) \,|\, ^7\text{Li}(3/2^-)\rangle$ overlaps from Fig. 4.

these methods may not yield the correct exponential asymptotic form given in Eq. (17), as is the case of methods employing harmonic oscillator bases [16,17]. In variational methods, including VMC, it may be hard to impose the correct asymptotics while preserving short-range properties. This problem is less prevalent in integral methods of computing ANCs in which the desired asymptotics is imposed by definition regardless of the actual asymptotic shape of the wave functions involved [13,20]. Second, ANCs extracted from Eq. (17) depend on the separation energy B. To determine ANCs from overlaps in a fully consistent manner, one should use the separation energy B_H obtained for a given Hamiltonian; however, for ANCs to be practically usable for reaction calculations, experimental values B_exp should be used. Ideally, $B_\text{H} \approx B_\text{exp}$, a condition that is often violated in literature and therefore relaxed without error analysis for ANCs [13,17,20]. We now discuss these aspects applied to GFMC.

It is gratifying to observe that the GFMC overlaps in Fig. 2 and Fig. 4 transition nicely from the interior into the asymptotic region and that in the computationally safe region ($r \lesssim 8$ fm) they follow closely the right asymptotic trend represented by the Whittaker functions. To illustrate this in more detail for overlaps from Figs. 2 and 4, we show in Fig. 5 the ratios

$$C(r) \equiv R(r)/[W_{-\eta,l+1/2}(2kr)/r]. \qquad (20)$$

Ideally, $C(r \to \infty)$ should approach C from Eq. (17), the ANC. As can be seen in the figure, the GFMC curves may not flatten out perfectly at larger distances where the method being driven by H' in Eq. (5) may break down because of insufficient contributions of the asymptotic part of the configuration space to the energy. To correct this imperfection, the GFMC overlaps are extended to larger distances by means of WS fits [Eq. (18)]. ANCs are then determined by applying Eq. (20) to GFMC overlap fits at large distances.

In GFMC, the binding energy is thought to be computed with systematic errors of about 1–2% [27,38,40]. Most GFMC overlaps in this work were obtained for the AV18 + IL7 potentials. For this potential, GFMC energies in Table I differ by less than 1% from experimental values, in most

cases the difference is less than 0.5%. These deviations, though being small fractions of total binding energies, may translate into bigger (fractional) deviations on core-valence separation energies, as can be seen from Tables II and III. Even then, however, the difference between experimental and GFMC separation energies is $\lesssim$3%, with a noticeable exception being the $\langle ^6\text{He}(0^+)\,|\,^7\text{He}(3/2^-)\rangle$ overlap involving a particle-unbound ^7He. For the latter overlap, the analog of the ANC is related to the decay width; in this work, we extract the ANCs only for particle-bound states of parent nuclei. Because GFMC wave functions are really eigenstates of H' rather than H, it is equally important to observe in Tables II and III that separation energies for these Hamiltonians are about the same (H' was adjusted to get $\langle H'\rangle \approx \langle H\rangle$, as mentioned in Sec. II B). To estimate the sensitivity of ANCs on separation energies, we refitted the GFMC overlaps from Figs. 2 and 4 with solutions of Eq. (18) imposing separation energies corresponding to $\pm 3\%$ deviations from B_exp. Using B_exp from Tables II and III, we obtain the following ANCs for $B = 0.97 B_\text{exp}$, $B = B_\text{exp}$, and $B = 1.03 B_\text{exp}$: -6.13, -6.45, and -6.78, respectively, for the $\langle ^3\text{H} \,|\, ^4\text{He}\rangle$ overlap and 3.33, 3.52, and 3.71, respectively, for the $\langle ^6\text{He} \,|\, ^7\text{Li}\rangle$ overlap. Thus, any uncertainty of about 3% or less on the separation energy translates into an ANC uncertainty of about 5–6% or less. Furthermore, the s-shell GFMC ANCs in Table VI agree well with those obtained within the HH method except for the weak d waves in $A = 3$ nuclei for which the two methods differ for unknown reasons (the HH ANCs assume the actual separation energies for a given Hamiltonian that are within a fraction of a percent of the experimental values). To test the dependence of GFMC ANCs in the p shell on starting VMC wave functions, we include in Table VII results involving the ground state of ^7Li obtained for several combinations of type I/II (see Sec. II A) trial wave functions; depending on the starting VMC wave function, GFMC ANCs differ by at most 7% in a given overlap channel.

Based on these arguments, we chose to fit GFMC overlaps and to determine the GFMC ANCs assuming experimental separation energies. We estimate the systematic errors on our ANCs to be $\lesssim$5%.

TABLE I. GFMC binding energies E for $A \leqslant 7$ nuclei for several $2N + 3N$ potentials H. Only statistical errors are shown on GFMC values. For p-shell nuclei, the VMC wave-function type is indicated. The energy shown for ^{2}H was obtained in a stochastic sampling of an explicit solution of Eq. (1). Experimental values are also shown.

$^A Z(J^\pi, T)$	Type	H	E (MeV)	
			GFMC	Exp.
^{2}H$(1^+, 0)$		AV18	$-2.2247(3)$	-2.2246
^{3}H$(\frac{1}{2}^+, \frac{1}{2})$		AV18 + IL7	$-8.47(0)$	-8.48
		AV18 + UIX	$-8.47(0)$	-8.48
^{3}He$(\frac{1}{2}^+, \frac{1}{2})$		AV18 + IL7	$-7.72(0)$	-7.72
		AV18 + UIX	$-7.72(0)$	-7.72
^{4}He$(0^+, 0)$		AV18 + IL7	$-28.43(0)$	-28.30
		AV18 + UIX	$-28.34(1)$	-28.30
^{6}He$(0^+, 1)$	I	AV18 + IL7	$-29.20(3)$	-29.27
^{6}Li$(1^+, 0)$	I	AV18 + IL7	$-31.93(3)$	-31.99
	II	AV18 + IL7	$-31.88(3)$	-31.99
^{6}Li$(3^+, 0)$	I	AV18 + IL7	$-29.59(3)$	-29.80
^{6}Li$(0^+, 1)$	I	AV18 + IL7	$-28.43(3)$	-28.43
^{7}He$(\frac{3}{2}^-, \frac{3}{2})$	I	AV18 + IL7	$-28.66(3)$	-28.83
^{7}Li$(\frac{3}{2}^-, \frac{1}{2})$	I	AV18 + IL7	$-39.08(3)$	-39.24
	II	AV18 + IL7	$-39.00(3)$	-39.24
^{7}Li$(\frac{1}{2}^-, \frac{1}{2})$	I	AV18 + IL7	$-38.88(3)$	-38.76
^{7}Be$(\frac{3}{2}^-, \frac{1}{2})$	I	AV18 + IL7	$-37.61(4)$	-37.60

For s-shell overlaps, $C(r)$ in Eq. (20) flatten out at $r \sim 2.5$–3 fm, where $C(r)/C \sim 0.9$, and they are almost fully converged at $r \sim 5$ fm; for p-shell overlaps, $C(r)/C \sim 0.9$ is realized at $r \sim 5$ fm. Therefore, the overlaps are (almost) asymptotic at about 5 fm, which is the upper radial limit used in our fitting procedure. We have checked that including the region beyond 5 fm in the fitting procedure does not result in significant changes of ANCs.

IV. RESULTS

In this section we present GFMC spectroscopic overlaps, SFs, and ANCs and compare them with those obtained by some other methods and with experimentally deduced values. A convenient parametrization of the overlaps is also provided.

Table I shows computed and experimental binding energies for $A \leqslant 7$ nuclear states relevant for this work. The errors shown in parentheses are only the Monte Carlo statistical errors; in addition, there may be systematic errors from the GFMC algorithm of the order of 1–2% [27,38,40]. Compared with previous GFMC works, the statistical accuracy on binding energies is much better thanks to the high sample counts needed for a statistically reliable sampling of overlap tails, as mentioned in Sec. III. Most GFMC results were obtained for the AV18 + IL7 potential. For this potential, GFMC energies in Table I differ by less than 1% from experimental values; in most cases the difference is less than 0.5%. For the ground states of ^{6}Li and ^{7}Li, both type I and type II VMC wave functions defined in Sec. II A were used. For comparison of GFMC overlaps with those obtained by other methods, we also constructed wave functions of s-shell nuclei bound by AV18 + UIX whose energies are also shown in Table I.

Besides getting the absolute binding energies right, it is important for consistent overlap calculations to work with nuclear states having the correct one-nucleon separation energies. In Tables II and III, we show GFMC one-nucleon separation energies computed for the desired Hamiltonian H from Eq. (1) and for the simplified H' from Eq. (5) along with experimental values. Given the agreement between GFMC and the experiment, and the related discussion in Sec. III, we assume the experimental separation energies when determining ANCs from GFMC overlaps and account for possible systematic errors inflicted by this choice.

Tables IV and V summarize, respectively, SFs for s- and p-shell nuclei with $A \leqslant 7$. In these tables, the errors on VMC and GFMC SFs are only statistical; possible systematic errors on GFMC values were estimated in Sec. III to be 2–3% or less.

In the s shell, where VMC wave functions are already very good approximations of true eigenstates [27], the $s_{1/2}$ SFs in Table IV change by less than 2% between VMC and GFMC. VMC, however, seems to underestimate the small amount of d waves in $A = 3$ nuclei by about 15%. Not surprising, s-shell results for AV18 + UIX and AV18 + IL7 are similar because both $3N$ forces, IL7 and especially UIX, were tuned to reproduce the binding of s-shell nuclei. The experimental information on SFs in the s shell is scarce; for the $\langle ^3$H $| ^4$He$\rangle$ overlap, the GFMC value of 1.61 is in good agreement

TABLE II. GFMC core-valence separation energies in the s shell for several $2N + 3N$ potentials H and for the corresponding H' from Eq. (5). The combined statistical errors on the core and the parent energies from Table I are all $\leqslant 0.01$ MeV. Experimental values are also shown.

Parent $^A Z(J^\pi, T)$	Core $^{A-1} Z(J^\pi, T)$	H	B (MeV)		
			GFMC, H	GFMC, H'	Exp.
^{3}H$(\frac{1}{2}^+, \frac{1}{2})$	^{2}H$(1^+, 0)$	AV18 + IL7	6.24	6.24	6.26
		AV18 + UIX	6.24	6.24	6.26
^{3}He$(\frac{1}{2}^+, \frac{1}{2})$	^{2}H$(1^+, 0)$	AV18 + IL7	5.49	5.49	5.49
		AV18 + UIX	5.50	5.50	5.49
^{4}He$(0^+, 0)$	^{3}H$(\frac{1}{2}^+, \frac{1}{2})$	AV18 + IL7	19.96	19.94	19.81
		AV18 + UIX	19.89	19.88	19.81
	^{3}He$(\frac{1}{2}^+, \frac{1}{2})$	AV18 + IL7	20.71	20.69	20.58
		AV18 + UIX	20.63	20.62	20.58

TABLE III. Same as Table II for $A \leqslant 7$ p-shell nuclei bound by AV18 + IL7. (Negative) Positive values mean that the A-body nucleus is particle (un)bound relative to the core. The VMC wave function type is indicated.

Parent		Core		B (MeV)		
$^A Z(J^\pi, T)$	Type	$^{A-1}Z(J^\pi, T)$	Type	GFMC, H	GFMC, H'	exp.
^{7}He$(\frac{3}{2}^-, \frac{3}{2})$	I	^{6}He$(0^+, 1)$	I	$-0.54(4)$	$-0.47(1)$	-0.45
^{7}Li$(\frac{3}{2}^-, \frac{1}{2})$	I	^{6}He$(0^+, 1)$	I	9.88(4)	9.82(1)	9.98
	II			9.81(4)	9.74(1)	9.98
	I	^{6}Li$(1^+, 0)$	I	7.15(4)	7.16(1)	7.25
	II		II	7.12(4)	7.06(1)	7.25
	I	^{6}Li$(3^+, 0)$	I	9.49(4)	9.45(1)	9.44
	II			9.42(4)	9.37(1)	9.44
	I	^{6}Li$(0^+, 1)$	I	10.65(4)	10.60(1)	10.81
	II			10.57(4)	10.52(1)	10.81
^{7}Li$(\frac{1}{2}^-, \frac{1}{2})$	I	^{6}Li$(1^+, 0)$	I	6.95(4)	7.00(1)	6.77
^{7}Be$(\frac{3}{2}^-, \frac{1}{2})$	I	^{6}Li$(1^+, 0)$	I	5.69(4)	5.68(2)	5.61
		^{6}Li$(3^+, 0)$	I	8.03(5)	7.98(2)	7.79
		^{6}Li$(0^+, 1)$	I	9.18(4)	9.13(2)	9.17

with an experimental value ~1.4–1.6 deduced from electron scattering [7].

The $A = 3$ nuclei contain 1.5 S, $T = 1, 0$ nucleon pairs [49,50]. The sums of s- and d-wave SFs for overlaps of ^{3}H and ^{3}He with a deuteron are about 1.32 and 1.33, respectively. If these values are interpreted as numbers of deuterons [51], it appears that about 90% of $T = 0$ pairs in $A = 3$ nuclei are in the deuteron state. We conjecture that the slightly bigger $\langle^2$H $|\,^3$He$\rangle$ SF compared with that between ^{2}H and ^{3}H is attributable to the fact that it is easier to compact a spatially extended deuteron into ^{3}He, which is somewhat bigger than the triton.

Using a similar probabilistic interpretation for ^{4}He, where all one-nucleon (neutron or proton) SFs add up to 2 [1] and those for overlaps with $A = 3$ nuclei in Table IV are about 1.6, we find that about 80% of all nucleon triples in ^{4}He are in the triton or ^{3}He state. Because both $A = 3$ nuclei are spatially more extended than ^{4}He and the triton is somewhat smaller

than ^{3}He, we conjecture that it is more likely to find a triton than ^{3}He inside ^{4}He, which is reflected by a slight difference in the corresponding SFs in Table IV. In the s shell, these conjectures are plausible because the s-wave SFs in Table IV account for such a big fraction of the total spectroscopic strength.

In Table IV, the AV18 + UIX values labeled HH are those of the HH method [47]; in particular, the overlaps for $A = 3$ parent nuclei are from [14] and those for ^{4}He are improved and updated versions of previously published results [15,48]. The HH results were converted to our conventions for overlaps. The agreement between GFMC and HH is very good, as can be seen from SFs in Table IV and from Fig. 6, where the actual $\langle^2$H $|\,^3$H$\rangle$ and $\langle^3$H $|\,^4$He$\rangle$ overlaps are shown. Small discrepancies exist between GFMC and HH overlaps at short distances, and the d-wave ANCs in $A = 3$ nuclei differ; the sources of these discrepancies remain

TABLE IV. SFs for overlaps between s-shell nuclei for a given $2N + 3N$ Hamiltonian H and angular momentum channel l_j. The statistical errors on VMC and GFMC values are less than 1 in the last digit shown; systematic uncertainties in GFMC values are 2–3% or less, as discussed in Sec. III. Also shown are the results of the HH method and experimentally deduced values.

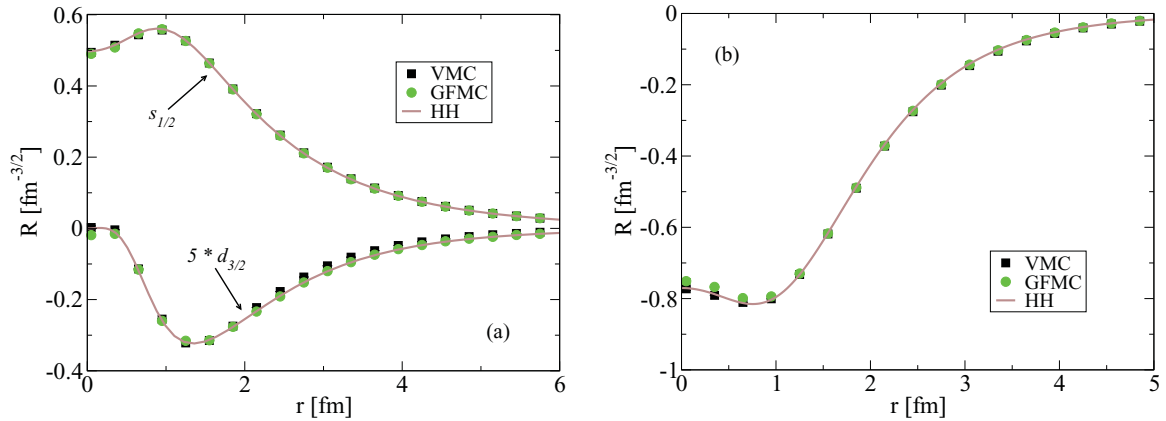| Parent	Core	l_j	H	S			
$^A Z(J^\pi, T)$	$^{A-1}Z(J^\pi, T)$			HH	VMC	GFMC	Exp.
^{3}H$(\frac{1}{2}^+, \frac{1}{2})$	^{2}H$(1^+, 0)$	$s_{1/2}$	AV18 + IL7		1.32	1.30	
			AV18 + UIX	1.30	1.32	1.30	
		$d_{3/2}$	AV18 + IL7		0.0194	0.0224	
			AV18 + UIX	0.0225	0.0195	0.0223	
^{3}He$(\frac{1}{2}^+, \frac{1}{2})$	^{2}H$(1^+, 0)$	$s_{1/2}$	AV18 + IL7		1.32	1.31	
			AV18 + UIX	1.31	1.32	1.31	
		$d_{3/2}$	AV18 + IL7		0.0190	0.0221	
			AV18 + UIX	0.0222	0.0191	0.0221	
^{4}He$(0+,0)$	^{3}H$(\frac{1}{2}^+, \frac{1}{2})$	$s_{1/2}$	AV18 + IL7		1.64	1.61	~1.4–1.6 [7]
			AV18 + UIX	1.60	1.63	1.61	
	^{3}He$(\frac{1}{2}^+, \frac{1}{2})$	$s_{1/2}$	AV18 + IL7		1.62	1.60	
			AV18 + UIX	1.58	1.62	1.60	

FIG. 6. (Color online) Comparison of the $s_{1/2}$ and the $d_{3/2}\langle^2\mathrm{H}\,|\,^3\mathrm{H}\rangle$ (a), and the $s_{1/2}\ \langle^3\mathrm{H}\,|\,^4\mathrm{He}\rangle$ (b) overlaps obtained for the AV18 + UIX potential within VMC, GFMC, and HH. Only statistical errors are shown on Monte Carlo overlaps.

unknown. An equally good agreement is obtained for overlaps involving $^3\mathrm{He}$.

As examples of our s-shell overlaps obtained for the AV18 + IL7 potential, we show in Fig. 7 the $\langle^2\mathrm{H}\,|\,^3\mathrm{H}\rangle$ and $\langle^3\mathrm{H}\,|\,^4\mathrm{He}\rangle$ overlaps. Also shown in these figures are WS fits of GFMC overlaps. Although the absolute overlap signs are rather arbitrary because they depend on the detailed construction of our wave functions, the order of vector couplings in Eqs. (8) and (9), and the isospin Clebsch-Gordan coefficient in Eq. (8), relative signs of different overlaps for a given parent-core combination may be important for interference effects. In our sign convention, the s- and d-wave overlaps in $A = 3$ nuclei have opposite signs consistent with experimentally deduced negative ratios of their ANCs shown in Table VI. Note the slight dips in s-wave overlaps near the origin that are consistent with a depletion of one-body densities of s-shell nuclei at short range [27] owing to a repulsive potential core.

VMC and GFMC SFs between $A = 6$ and $A = 7$ p-shell nuclei bound by AV18 + IL7 are listed in Table V along with shell-model predictions and experimentally deduced values. The Cohen and Kurath [44] shell-model (SM) values in Table V were corrected for center-of-mass motion effects by a factor

$A/(A − 1)$ [5,52] to make them comparable with our results, which, as mentioned in Sec. II C, are free of such spurious contaminations. In addition, a square of the isospin coupling coefficient from Eq. (8) was factored into SM values in Table V. Because it is not clear whether experimental SFs, often compared by their authors with original shell-model values of Ref. [44], were corrected backward for center-of-mass effects or not, we quote them as they appear in the literature.

In the p shell, the structure improvement provided by GFMC over VMC is known to be more significant compared with the s shell [27]. This is reflected by SFs in Table V that change by as much as 15% between VMC and GFMC. The results involving the ground states of $^6\mathrm{Li}$ and $^7\mathrm{Li}$ for which both type I and type II VMC wave functions were used demonstrate that, by closing the gap between VMC SFs as big as ∼20% down to less than 3%, the GFMC method is rather insensitive to starting trial functions.

In Table V, the experimental SFs from Ref. [26] are based on electron scattering data; the other experimental values were deduced from hadronic reactions. The experimental SFs from Ref. [23] listed in the table are only relative; the authors of
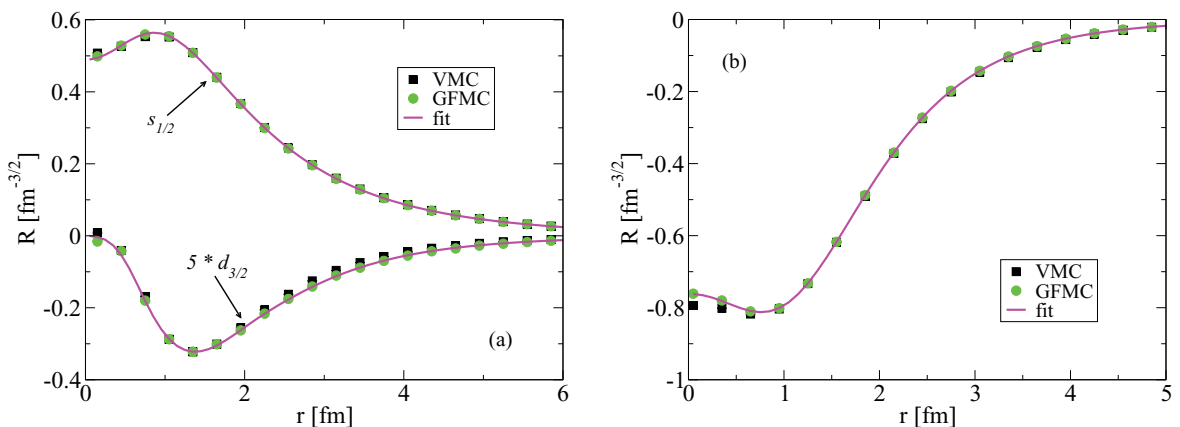

FIG. 7. (Color online) VMC and GFMC $s_{1/2}$ and $d_{3/2}\langle^2\mathrm{H}\,|\,^3\mathrm{H}\rangle$ (a) and $s_{1/2}\langle^3\mathrm{H}\,|\,^4\mathrm{He}\rangle$ (b) overlaps obtained for the AV18 + IL7 potential. Only statistical errors are shown. Also shown are WS fits of GFMC overlaps.

TABLE V. SFs for overlaps between $A = 6$ and $A = 7$ p-shell nuclei for the AV18 + IL7 potential in angular momentum channels l_j. The VMC and GFMC statistical errors are insignificant compared with the estimated systematic uncertainties of 2–3% or less for GFMC, as discussed in Sec. III. SM denotes corrected shell-model values (see text). Experimentally deduced values are also shown.

Parent		Core		l_j	S			
$^A Z(J^\pi, T)$	Type	$^{A-1} Z(J^\pi, T)$	Type		SM	VMC	GFMC	Exp.
$^7\mathrm{He}(\frac{3}{2}^-, \frac{3}{2})$	I	$^6\mathrm{He}(0^+, 1)$	I	$p_{3/2}$	0.690	0.532	0.565	0.37(7) [21]
$^7\mathrm{Li}(\frac{3}{2}^-, \frac{1}{2})$	I	$^6\mathrm{He}(0^+, 1)$	I	$p_{3/2}$	0.691	0.442	0.406	0.44(6)^a [23], 0.42(4) [26]
	II					0.365	0.409	
	I	$^6\mathrm{He}(2^+, 1)$	I	$p_{1/2}$	0.253	0.128		
				$p_{3/2}$	0.212	0.146		
				Sum	0.466	0.274		0.16(2) [26]
	I	$^6\mathrm{Li}(1^+, 0)$	I	$p_{1/2}$	0.338	0.229	0.230	
				$p_{3/2}$	0.503	0.480	0.438	
				Sum	0.841	0.709	0.668	0.74(11)^a [23], 0.73(5) [53]
	II		II	$p_{1/2}$	0.338	0.211	0.229	
				$p_{3/2}$	0.503	0.401	0.428	
				Sum	0.841	0.612	0.657	0.74(11)^a [23], 0.73(5) [53]
	I	$^6\mathrm{Li}(3^+, 0)$	I	$p_{3/2}$	0.646	0.500	0.435	0.72(14) [54], 0.58(13) [55]
	II					0.436	0.447	
	I	$^6\mathrm{Li}(0^+, 1)$	I	$p_{3/2}$	0.345	0.221	0.203	0.19(3)^a [23]
	II					0.183	0.204	
$^7\mathrm{Li}(\frac{1}{2}^-, \frac{1}{2})$	I	$^6\mathrm{Li}(1^+, 0)$	I	$p_{1/2}$	0.045	0.069	0.060	
				$p_{3/2}$	0.997	0.854	0.759	
				Sum	1.042	0.923	0.819	1.15 [56], 0.90(9) [53]
$^7\mathrm{Be}(\frac{3}{2}^-, \frac{1}{2})$	I	$^6\mathrm{Li}(1^+, 0)$	I	$p_{1/2}$	0.338	0.229	0.225	
				$p_{3/2}$	0.503	0.480	0.438	
				Sum	0.841	0.709	0.663	
		$^6\mathrm{Li}(3^+, 0)$	I	$p_{3/2}$	0.646	0.500	0.457	
		$^6\mathrm{Li}(0^+, 1)$	I	$p_{3/2}$	0.345	0.221	0.210	

^{a}Values obtained from $(\sigma_{\mathrm{exp}}/\sigma_{\mathrm{DWBA}}) \times 0.32$; see text.

that work concluded that their data analysis cannot be trusted to provide an absolute determination of cross sections, and only relative SFs for several reactions were provided upon a renormalization by a somewhat arbitrary factor of 0.32, making them comparable to theoretical VMC values available at the time. In Ref. [26], SFs deduced from electron-induced proton knockout on ^{7}Li leading to the two lowest states of ^{6}He were found in perfect agreement with VMC values available at the time; in Table V, the GFMC SFs involving ^{6}He(0^+) still agree perfectly with experiment, but the agreement for the reaction leading to ^{6}He(2^+) has been spoiled by an error in the VMC code discovered after the original work [26] had been published. The $\langle {}^6\mathrm{He}(2^+) | {}^7\mathrm{Li}(3/2^-) \rangle$ overlap involves an unbound state of ^{6}He for which GFMC does not find a stable energy; instead, the method produces the core nucleus with an ever-increasing radius by breaking it gradually into ^{4}He and two neutrons. Consequently, the GFMC SFs for this overlap steadily decrease and as such are absent in Table V. Given the experimental and systematic GFMC uncertainties and bearing in mind all the issues related to the meaning of spectroscopic overlaps and factors mentioned in Sec. I, we conclude that the GFMC results in Table V seem to support newer determinations of (relative) SFs.

We do not find a significant difference between SFs of mirror nuclei ^{7}Li and ^{7}Be; also, SFs between the ground state

of ^{7}Li and the $J^\pi, T = 0^+$, 1 isobaric analogs of ^{6}He and ^{6}Li differ just by a factor of 2 owing to the difference in isospin coupling coefficients in Eq. (8). Our SFs for overlaps between $A = 6$ and $A = 7$ nuclei suggest a substantial quenching of shell-model values by as much as 40% (except for the weak $p_{1/2}$ channel of the $\langle {}^6\mathrm{Li}(1^+) | {}^7\mathrm{Li}(1/2^-) \rangle$ overlap).

As examples of p-shell overlaps, Fig. 8 shows the $p_{1/2}$ and $p_{3/2}$ $\langle {}^6\mathrm{Li}(1^+) | {}^7\mathrm{Li}(3/2^-) \rangle$ overlaps obtained for the AV18 + IL7 interaction with GFMC wave functions originating from type I VMC functions (see Fig. 4 for another example). Also shown in the figure are WS fits of GFMC overlaps. The figure illustrates that the overlaps may change from VMC to GFMC even when their SFs remain the same ($p_{1/2}$ channel); however, sometimes the change in SFs is more attributable to a renormalization than a shape change ($p_{3/2}$ channel). To better appreciate where the changes in SFs come from, we superimpose in Fig. 8 the "density" functions $(R \times r)^2$ whose integral in Eq. (11) gives the SFs.

The $\langle {}^6\mathrm{He} | {}^7\mathrm{He} \rangle$ overlap in Table V is particularly challenging for both theory and experiment because it involves a parent nucleus that is particle unbound by about 450 keV relative to the core. In our calculations, ^{7}He is treated as a bound state and the GFMC propagation yields a stable energy and separation energy shown in Tables I and III. Despite the bound-state approximation to ^{7}He, GFMC substantially

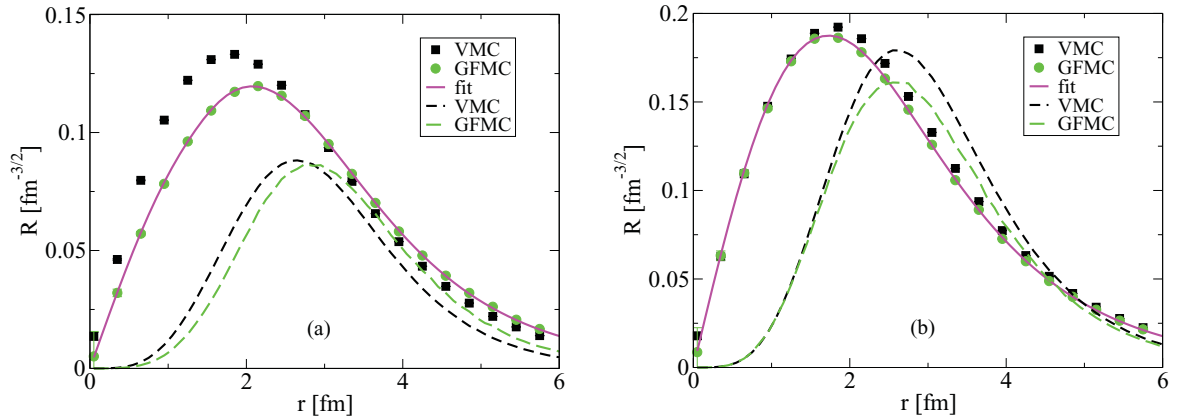FIG. 8. (Color online) VMC and GFMC $p_{1/2}$ (a) and $p_{3/2}$ (b) $\langle {}^6\mathrm{Li}(1^+) \,|\, {}^7\mathrm{Li}(3/2^-)\rangle$ overlaps obtained for the AV18 + IL7 potential. Only statistical errors are shown. Also shown are WS fits of GFMC overlaps. Superimposed as dashed lines are the "density" functions $(R \times r)^2$.

improves the overlap tail compared with VMC, as can be seen in Fig. 9, where the desired asymptotic form is represented by the scattering Coulomb function plotted at 90° phase shift.

ANCs, extracted from GFMC overlaps by a fitting procedure outlined in Sec. III, are listed in Tables VI and VII for s- and p-shell nuclei along with experimentally derived numbers and those of some other realistic methods. Systematic errors on our ANCs were estimated in Sec. III to be $\lesssim 5\%$. As was mentioned earlier in this section, the absolute signs of GFMC overlaps and ANCs are not meaningful, but relative signs in different overlap channels for a given parent-core combination matter.

In the s shell, GFMC and HH overlaps obtained for the AV18 + UIX force agree well (see Fig. 6), and so do ANCs in Table VI except for the weak d waves in $A = 3$ nuclei (and consequently for the ratios of d- to s-wave ANCs), for which the two methods differ for unknown reasons. The HH ANCs assume the actual separation energies for a given Hamiltonian, which are close to the experimental values, and so the ANCs would not change dramatically if experimental

FIG. 9. (Color online) VMC and GFMC $p_{3/2}\langle {}^6\mathrm{He}(0^+) \,|\, {}^7\mathrm{He}(3/2^-)\rangle$ overlaps obtained for the AV18 + IL7 potential. Only statistical errors are shown. Also shown is the irregular Coulomb function $G(r)/r$ for the experimental separation energy representing the scattering asymptotics at 90° phase shift.

separation energies were used instead. In Ref. [20], an integral method (IM) was used to compute ANCs in $A \leqslant 9$ nuclei from AV18 + UIX VMC wave functions assuming experimental core-valence separation energies; in Table VI, these ANCs are labeled VMC-IM. For the dominant s-wave channels, VMC-IM results are in a good agreement with ours. However, the difference between GFMC and VMC-IM ANCs for the weaker d-waves in $A = 3$ nuclei, larger than 15%, is outside of the systematic error bars set on GFMC ANCs; this discrepancy is most likely attributable to VMC wave functions employed by VMC-IM that, as shown in Table IV in terms of SFs, underestimate the strength of d waves in $A = 3$ nuclei. Our ANCs are in a fair agreement with some experimental values but differ from others. Experimentally, particular emphasis was put on the ratio of d- to s-wave ANCs in ${}^3\mathrm{H}$ and ${}^3\mathrm{He}$ most precisely inferred from tensor analyzing powers; the experimental values listed in Table VI agree well with ours, including the relative negative phase.

As shown in Table VII, ANCs for overlaps between $A = 6$ and $A = 7$ nuclei are constrained rather poorly experimentally. In general, ANCs in the lower p-shell are determined mostly from hadronic processes, such as transfer or knockout reactions; see Refs. [13,20] and references therein. In Table VII, we show the full range of experimental ANCs from [63] for overlaps between the ground state of ${}^7\mathrm{Li}$ and the lowest states in ${}^6\mathrm{Li}$. Overall, given the experimental uncertainties, it is hard to compare GFMC to experiment. ANCs calculated within VMC-IM for AV18 + UIX are in a broad agreement with our AV18 + IL7 results, though with some notable differences especially for the $p_{3/2}$ $\langle {}^6\mathrm{Li}(1^+) \,|\, {}^7\mathrm{Li}(3/2^-)\rangle$ overlap. Based on simple analytical arguments, the ratio of $\langle {}^6\mathrm{Li}(1^+) \,|\, {}^7\mathrm{Be}(3/2^-)\rangle$ and $\langle {}^6\mathrm{Li}(1^+) \,|\, {}^7\mathrm{Li}(3/2^-)\rangle$ ANCs involving mirror nuclei ${}^7\mathrm{Be}$ and ${}^7\mathrm{Li}$ was predicted to be 1.02 for both $p_{1/2}$ and $p_{3/2}$ channels [64]. We obtain 0.95(7) for the $p_{1/2}$ channel and 0.98(7) for the $p_{3/2}$ channel assuming 5% errors on GFMC ANCs, using averaged type I and type II $\langle {}^6\mathrm{Li}(1^+) \,|\, {}^7\mathrm{Li}(3/2^-)\rangle$ ANCs from Table VII, and disregarding the signs of involved ANCs.

Finally, we present in Table VIII potential parameters appearing in Eq. (18) that provide good fits to GFMC overlaps. These fits were used to extract ANCs. They also
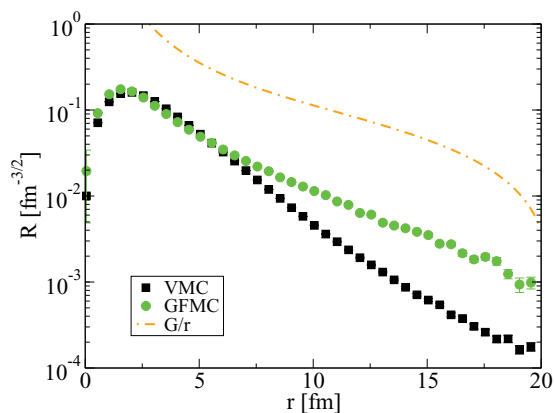
TABLE VI. ANCs for GFMC overlaps between s-shell nuclei for a given $2N + 3N$ Hamiltonian H and angular momentum channel l_j. Systematic uncertainties on GFMC values are 5% or less, as discussed in Sec. III. Also shown are the results of the HH and VMC-IM methods and experimentally deduced values. The errors on VMC-IM are only statistical. For $A = 3$ nuclei, ratios of d- to s-wave ANCs are also shown.

Parent	Core	l_j	H	C (fm$^{-1/2}$)			
$^A Z(J^\pi, T)$	$^{A-1} Z(J^\pi, T)$			HH	VMC-IM	GFMC	Exp.
^{3}H($\frac{1}{2}^+$, $\frac{1}{2}$)	^{2}H(1^+, 0)	$s_{1/2}$	AV18 + IL7			2.14	2.11(3) [57], 2.07(2) [13], 1.87(14) [58]
			AV18 + UIX	2.15	2.13(1)	2.14	
		$d_{3/2}$	AV18 + IL7			−0.0848	
			AV18 + UIX	−0.0925	−0.0979(9)	−0.0842	
		C_d/C_s	AV18 + IL7			−0.0396	−0.0418(15) [59]
			AV18 + UIX	−0.0430	−0.0460(5)	−0.0393	
^{3}He($\frac{1}{2}^+$, $\frac{1}{2}$)	^{2}H(1^+, 0)	$s_{1/2}$	AV18 + IL7			2.10	2.10(16) [58], 1.76(11) [60]
			AV18 + UIX	2.16	2.14(1)	2.10	
		$d_{3/2}$	AV18 + IL7			−0.0762	
			AV18 + UIX	−0.0865	−0.0927(10)	−0.0794	
		C_d/C_s	AV18 + IL7			−0.0363	−0.0389(42) [59]
			AV18 + UIX	−0.0400	−0.0432(5)	−0.0378	
^{4}He(0^+, 0)	^{3}H($\frac{1}{2}^+$, $\frac{1}{2}$)	$s_{1/2}$	AV18 + IL7			−6.45	7.36(19) [58], 6.70(50) [58], 5.44(15) [61]
			AV18 + UIX	−6.47	−6.55(2)	−6.49	
	^{3}He($\frac{1}{2}^+$, $\frac{1}{2}$)	$s_{1/2}$	AV18 + IL7			6.45	6.77(51) [58], 6.52(49) [58]
			AV18 + UIX	6.36	6.42(2)	6.49	

allow our results to be easily used in DWBA or CCBA reaction calculations [45,46]. Besides setting the core-valence separation energies to their experimental values, no other constraints were imposed in the fitting procedure. In the s shell, we found it necessary to introduce a short-range repulsive Gaussian potential term to reproduce dips in GFMC overlaps near the origin as seen in Fig. 7; in the p shell, such a term is not necessary. Good fits to d-wave overlaps in $A = 3$ nuclei seem to require very strong repulsive potential cores and negative radii of the central WS part. Also, for d waves the first few

TABLE VII. ANCs for GFMC overlaps between $A = 6$ and $A = 7$ p-shell nuclei for the AV18 + IL7 potential in angular momentum channels l_j. Systematic uncertainties on GFMC values are 5% or less as discussed in Sec. III. Results of the VMC-IM method for AV18 + UIX with statistical errors only and experimentally deduced values are also shown.

Parent		Core		l_j	C (fm$^{-1/2}$)		
$^A Z(J^\pi, T)$	Type	$^{A-1} Z(J^\pi, T)$	Type		VMC-IM	GFMC	Exp.
^{7}Li($\frac{3}{2}^-$, $\frac{1}{2}$)	I	^{6}He(0^+, 1)	I	$p_{3/2}$	3.68(5)	3.52	2.48 [62]
	II					3.65	
	I	^{6}Li(1^+, 0)	I	$p_{1/2}$	1.65(1)	1.73	
				$p_{3/2}$	1.89(1)	2.29	
				$\sqrt{\sum C^2}$	2.51(1)	2.87	1.26–2.82 [63]
	II		II	$p_{1/2}$		1.85	
				$p_{3/2}$		2.20	
				$\sqrt{\sum C^2}$		2.87	1.26–2.82 [63]
	I	^{6}Li(3^+, 0)	I	$p_{3/2}$		3.50	2.06–3.00 [63]
	II					3.63	
	I	^{6}Li(0^+, 1)	I	$p_{3/2}$		−2.39	1.71–2.62 [63]
	II					−2.46	
^{7}Li($\frac{1}{2}^-$, $\frac{1}{2}$)	I	^{6}Li(1^+, 0)	I	$p_{1/2}$	−0.543(16)	−0.573	
				$p_{3/2}$	−2.54(4)	−2.85	
				$\sqrt{\sum C^2}$	2.60(4)	2.91	
^{7}Be($\frac{3}{2}^-$, $\frac{1}{2}$)	I	^{6}Li(1^+, 0)	I	$p_{1/2}$	−1.87(3)	−1.70	
				$p_{3/2}$	−2.15(3)	−2.20	
				$\sqrt{\sum C^2}$	2.85(3)	2.78	
		^{6}Li(3^+, 0)	I	$p_{3/2}$		−3.49	
		^{6}Li(0^+, 1)	I	$p_{3/2}$		−2.58	

TABLE VIII. Fitting parameters from Eq. (18) for GFMC overlaps obtained for the AV18 + IL7 potential in angular momentum channels l_j. All p-shell overlaps originated from type I VMC wave functions. The precise values of $V_{\rm WS}$ are adjusted to reproduce the experimental separation energies $B_{\rm exp}$.

Parent $^A Z(J^\pi, T)$	Core $^{A-1} Z(J^\pi, T)$	l_j	$V_{\rm WS}$ (MeV)	$R_{\rm WS}$ (fm)	$a_{\rm WS}$ (fm)	β 0.00	ρ (fm)	$V_{\rm so}$ (MeV)	$R_{\rm so}$ (fm)	$a_{\rm so}$ (fm)	$B_{\rm exp}$ (MeV)
^{3}H($\frac{1}{2}^+$, $\frac{1}{2}$)	^{2}H(1^+, 0)	$s_{1/2}$	−172.88	0.56	0.69	1.15	0.64				6.2572
		$d_{3/2}$	−2732.90	−1.15	0.91	1.16	0.41	2.95	2.15	0.14	6.2572
^{3}He($\frac{1}{2}^+$, $\frac{1}{2}$)	^{2}H(1^+, 0)	$s_{1/2}$	−179.94	0.54	0.68	1.13	0.64				5.4934
		$d_{3/2}$	−8155.10	−2.19	0.91	1.03	0.35	1.47	2.07	0.06	5.4934
^{4}He(0^+, 0)	^{3}H($\frac{1}{2}^+$, $\frac{1}{2}$)	$s_{1/2}$	−202.21	0.93	0.66	0.87	0.81				19.814
	^{3}He($\frac{1}{2}^+$, $\frac{1}{2}$)	$s_{1/2}$	−200.93	0.88	0.69	0.87	0.79				20.578
^{7}Li($\frac{3}{2}^-$, $\frac{1}{2}$)	^{6}He(0^+, 1)	$p_{3/2}$	−58.93	2.68	0.93			1.26	0.91	0.07	9.9758
	^{6}Li(1^+, 0)	$p_{1/2}$	−41.80	3.18	0.85			2.45	1.35	0.17	7.25
		$p_{3/2}$	−69.55	1.89	1.17			2.13	2.36	0.21	7.25
	^{6}Li(3^+, 0)	$p_{3/2}$	−62.98	2.35	1.18			1.72	0.55	0.09	9.436
	^{6}Li(0^+, 1)	$p_{3/2}$	−59.39	2.64	0.97			0.93	0.91	0.22	10.813
^{7}Li($\frac{1}{2}^-$, $\frac{1}{2}$)	^{6}Li(1^+, 0)	$p_{1/2}$	−33.71	3.39	0.31			1.44	1.09	0.03	6.772
		$p_{3/2}$	−65.00	2.04	1.15			1.14	0.88	0.03	6.772
^{7}Be($\frac{3}{2}^-$, $\frac{1}{2}$)	^{6}Li(1^+, 0)	$p_{1/2}$	−39.45	3.32	0.76			3.47	1.44	0.39	5.6055
		$p_{3/2}$	−72.22	1.85	1.11			2.62	2.53	0.31	5.6055
	^{6}Li(3^+, 0)	$p_{3/2}$	−59.20	2.52	1.07			1.08	0.79	0.03	7.7915
	^{6}Li(0^+, 1)	$p_{3/2}$	59.49	2.64	0.96			1.06	1.05	0.03	9.1685

radial bins were omitted from the fit because they are rather uncertain. To reproduce the results presented in this work, the WS fits need to be normalized to SFs from Tables IV and V. Our GFMC overlaps are available from Ref. [19].

V. SUMMARY AND CONCLUSIONS

We have reported GFMC calculations of one-nucleon spectroscopic overlaps in nuclei with mass numbers $A \leqslant 7$. The calculations have used wave functions derived from a realistic Hamiltonian that reproduces well the low-lying spectra of light nuclei. The overlaps are extrapolated from mixed estimates between VMC and GFMC wave functions, and they are extended to regions beyond the nuclear surface, where the GFMC method may not be accurate, by means of WS fits to the overlap interior. A goal of this work is to provide a consistent set of spectroscopic overlaps, SFs, and ANCs in light nuclei, obtained from our currently best GFMC wave functions, that can be used as structure input in analyzing existing or future experimental data.

The comparison of SFs and ANCs with experimentally deduced values is obscured, as mentioned in Sec. I, by the model-dependent way these quantities are extracted from experimental data and by the issues related to the meaning of spectroscopic overlaps. For many overlaps, it is hard to judge the agreement or disagreement between theory and experiment because of the nonexisting or conflicting experimental values. Our (relative) SFs seem to broadly support more recent values deduced from hadronic processes, and some agree particularly well with values provided by electron-scattering experiments. Our calculations reproduce, within error bars, the experimentally well-deduced ratios of d- to s-wave ANCs in $A = 3$ nuclei. We observe a rather substantial (up to 40%) quenching of GFMC SFs when compared with the traditional shell model. The GFMC improves the VMC overlaps, but the corrections to SFs are sufficiently small, indicating that the VMC values used to analyze experimental data in Refs. [21–26] were reliable.

The GFMC overlaps presented in this paper are available from Ref. [19]. The overlaps for somewhat heavier nuclei up to $A \lesssim 10$ will be the subject of a forthcoming paper.

[1] C. F. Clement, Nucl. Phys. A **213**, 469 (1973).

[2] J. M. Bang, F. G. Gareev, W. T. Pinkston, and J. S. Vaagen, Phys. Rep. **125**, 253 (1985).

[3] M. H. Macfarlane and J. B. French, Rev. Mod. Phys. **32**, 567 (1960).

[4] G. R. Satchler, *Direct Nuclear Reactions* (Oxford University Press, London, 1983).

[5] P. G. Hansen and J. A. Tostevin, Annu. Rev. Nucl. Part. Sci. **53**, 219 (2003).

[6] I. Thompson and F. M. Nunes, *Nuclear Reactions for*

Astrophysics (Cambridge University Press, New York, 2009).

[7] V. R. Pandharipande, I. Sick, and P. K. A. deWitt Huberts, Rev. Mod. Phys. **69**, 981 (1997).

[8] G. J. Kramer, H. P. Blok, and L. Lapikás, Nucl. Phys. A **679**, 267 (2001).

[9] R. Beck, F. Dickmann, and R. G. Lovas, Ann. Phys. **173**, 1 (1987).

[10] A. M. Mukhamedzhanov and A. S. Kadyrov, Phys. Rev. C **82**, 051601 (2010).

[11] J. Lee, J. A. Tostevin, B. A. Brown, F. Delaunay, W. G. Lynch, M. J. Saelim, and M. B. Tsang, Phys. Rev. C **73**, 044608 (2006).

[12] C. Bisconti, F. Arias de Saavedra, and G. Co', Phys. Rev. C **75**, 054302 (2007).

[13] N. K. Timofeyuk, Phys. Rev. C **81**, 064306 (2010).

[14] A. Kievsky, S. Rosati, M. Viviani, C. R. Brune, H. J. Karwowski, E. J. Ludwig, and M. H. Wood, Phys. Lett. B **406**, 292 (1997).

[15] M. Viviani, A. Kievsky, and S. Rosati, Phys. Rev. C **71**, 024006 (2005).

[16] P. Navrátil, Phys. Rev. C **70**, 054324 (2004).

[17] P. Navrátil, C. A. Bertulani, and E. Caurier, Nucl. Phys. A **787**, 539 (2007).

[18] O. Jensen, G. Hagen, T. Papenbrock, D. J. Dean, and J. S. Vaagen, Phys. Rev. C **82**, 014310 (2010).

[19] [http://www.phy.anl.gov/theory/research/overlap/].

[20] K. M. Nollett and R. B. Wiringa, Phys. Rev. C **83**, 041001 (2011).

[21] A. H. Wuosmaa *et al.* Phys. Rev. Lett. **94**, 082502 (2005).

[22] A. H. Wuosmaa *et al.*, Phys. Rev. C **72**, 061301 (2005).

[23] A. H. Wuosmaa *et al.*, Phys. Rev. C **78**, 041302 (2008).

[24] R. Kanungo *et al.*, Phys. Lett. B **660**, 26 (2008).

[25] G. F. Grinyer *et al.*, Phys. Rev. Lett. **106**, 162502 (2011).

[26] L. Lapikás, J. Wesseling, and R. B. Wiringa, Phys. Rev. Lett. **82**, 4404 (1999).

[27] S. C. Pieper and R. B. Wiringa, Annu. Rev. Nucl. Part. Sci. **51**, 53 (2001).

[28] S. C. Pieper, K. Varga, and R. B. Wiringa, Phys. Rev. C **66**, 044310 (2002).

[29] S. C. Pieper, R. B. Wiringa, and J. Carlson, Phys. Rev. C **70**, 054325 (2004).

[30] S. C. Pieper, Nucl. Phys. A **751**, 516 (2005).

[31] K. M. Nollett, S. C. Pieper, R. B. Wiringa, J. Carlson, and G. M. Hale, Phys. Rev. Lett. **99**, 022502 (2007).

[32] M. Pervin, S. C. Pieper, and R. B. Wiringa, Phys. Rev. C **76**, 064319 (2007).

[33] L. E. Marcucci, M. Pervin, S. C. Pieper, R. Schiavilla, and R. B. Wiringa, Phys. Rev. C **78**, 065501 (2008).

[34] R. B. Wiringa, V. G. J. Stoks, and R. Schiavilla, Phys. Rev. C **51**, 38 (1995).

[35] S. C. Pieper, AIP Conf. Proc. **1011**, 143 (2008).

[36] B. S. Pudliner, V. R. Pandharipande, J. Carlson, and R. B. Wiringa, Phys. Rev. Lett. **74**, 4396 (1995).

[37] N. Metropolis, A. W. Rosenbluth, M. N. Rosenbluth, A. H. Teller, and E. Teller, J. Chem. Phys. **21**, 1087 (1953).

[38] R. B. Wiringa, S. C. Pieper, J. Carlson, and V. R. Pandharipande, Phys. Rev. C **62**, 014001 (2000).

[39] R. B. Wiringa, Phys. Rev. C **43**, 1585 (1991).

[40] B. S. Pudliner, V. R. Pandharipande, J. Carlson, S. C. Pieper, and R. B. Wiringa, Phys. Rev. C **56**, 1720 (1997).

[41] M. Abramowitz and I. A. Stegun, *Handbook of Mathematical Functions* (Dover, New York, 1972).

[42] K. M. Nollett, R. B. Wiringa, and R. Schiavilla, Phys. Rev. C **63**, 024003 (2001).

[43] K. M. Nollett, Phys. Rev. C **63**, 054002 (2001).

[44] S. Cohen and D. Kurath, Nucl. Phys. A **101**, 1 (1967).

[45] M. H. Macfarlane and S. Pieper, Argonne National Laboratory Report ANL-76-11, Rev. 1, 1978.

[46] I. J. Thompson, Comput. Phys. Rep. **7**, 167 (1988).

[47] A. Kievsky, S. Rosati, M. Viviani, L. E. Marcucci, and L. Girlanda, J. Phys. G: Nucl. Part. Phys. **35**, 063101 (2008).

[48] M. Viviani and A. Kievsky (private communication).

[49] J. L. Forest, V. R. Pandharipande, S. C. Pieper, R. B. Wiringa, R. Schiavilla, and A. Arriaga, Phys. Rev. C **54**, 646 (1996).

[50] R. B. Wiringa, Phys. Rev. C **73**, 034317 (2006).

[51] R. Schiavilla, V. R. Pandharipande, and R. B. Wiringa, Nucl. Phys. A **449**, 219 (1986).

[52] A. E. L. Dieperink and T. de Forest, Phys. Rev. C **10**, 543 (1974).

[53] S. Jun *et al.*, Chin. Phys. Lett. **27**, 052101 (2010).

[54] T. Y. Li and S. K. Mark, Nucl. Phys. A **123**, 147 (1969).

[55] I. S. Towner, Nucl. Phys. A **126**, 97 (1969).

[56] J. P. Schiffer, G. C. Morrison, R. H. Siemssen, and B. Zeidman, Phys. Rev. **164**, 1274 (1967).

[57] B. A. Girard and M. G. Fuda, Phys. Rev. C **19**, 583 (1979).

[58] M. P. Locher and T. Mizutani, Phys. Rep. **46**, 43 (1978).

[59] J. E. Purcell, J. H. Kelley, E. Kwan, C. G. Sheu, and H. R. Weller, Nucl. Phys. A **848**, 1 (2010).

[60] A. V. Blinov *et al.*, J. Phys. G: Nucl. Phys. **11**, 623 (1985).

[61] L. D. Blokhintsev, I. Borbely, and E. I. Dolinskii, Sov. J. Part. Nucl. **8**, 485 (1977) [Fiz. Elem. Chastits At. Yadra **8**, 1189 (1977)].

[62] S. M. Bekbaev, G. Kim, A. M. Mukhamedzhanov, and N. K. Timofeyuk, Sov. J. Nucl. Phys. **54**, 232 (1991).

[63] I. R. Gulamov, A. M. Mukhamedzhanov, and G. K. Nie, Phys. At. Nucl. **58**, 1689 (1995) [Yad. Fiz. **58**, 1789 (1995)].

[64] N. K. Timofeyuk, R. C. Johnson, and A. M. Mukhamedzhanov, Phys. Rev. Lett. **91**, 232501 (2003).